An Algebraic Algorithm for Motor Voltage Waveform Prediction in Dual-LCI Drives With Interconnected DC-Links

Sobhan Mohamadian, Simone Castellan, Alberto Tessarolo, *Senior Member, IEEE*,
Giancarlo Ferrari, and Abbas Shoulaie

Abstract—Load-commutated inverters (LCI's) are often used to supply dual-three-phase synchronous motors in high-power variable-speed applications. A pair of LCIs is used in this arrangement to feed the two motor three-phase winding sets. In order to cope with inter-harmonic issues, a drive configuration with an interconnection of the two LCI dc-links has been proposed. In this paper, such a drive design is shown to produce an increased voltage stress on motor windings compared with traditional configurations. The problem is investigated in the paper by proposing an algebraic algorithm capable of predicting the steady-state voltage waveform applied to the motor terminals and arising between the star points of the two winding sets. Unlike conventional dynamic simulations, the proposed approach gives practically instantaneous results, making it possible to quickly investigate a wide number of possible operating conditions. Furthermore, it requires a limited knowledge of system parameters, which are often hardly available. Its reliability and accuracy are assessed by comparison with measurements on a test drive system and examples are given of the method application to the sizing of motor insulation system.

Index Terms—DC-link interconnection, load-commutated inverters, motor winding insulation, split-phase motors.

I. INTRODUCTION

HIGH RELIABILITY, simple structure, inherent short-circuit protection and low cost are some major advantages of load-commutated inverter (LCI)-fed wound-field synchronous machines (WFSM's) which are frequently used in high-power medium-voltage applications such as pumps, compressors, gas turbine starters and ships propulsion [1]–[3].

In spite of its several advantages, LCI technology suffers from well-known drawbacks such as torque pulsations as well as line-side and motor-side current harmonics and inter-harmonics [4], [5]. The motor torque quality can be remarkably enhanced by adopting a split-phase WFSM fed by multiple LCI's [6], [7]. The most common configuration includes a dual-three-phase

S. Mohamadian and A. Shoulaie are with the Department of Electrical Engineering, Iran University of Science and Technology, Tehran 16846-13114, Iran (e-mail: s_mohamadian@iust.ac.ir; shoulaie@iust.ac.ir).

S. Castellan and A. Tessarolo are with the Department of Engineering and Architecture, University of Trieste, Trieste 34128, Italy (e-mail: scastellan@units.it; atessarolo@units.it).

G. Ferrari is with the NIDEC-ASI, Milan 20126, Italy (e-mail: Giancarlo.ferrari@nidec-asi.com).

machine and two LCI's wherein the sixth harmonic torque component is removed [8]. Furthermore, this technology allows for using multi-pulse rectifiers to reduce grid-side harmonic pollution [9].

However, inter-harmonic current components, whose frequencies are not integer multiples of the fundamental one, appear when the grid and motor operating frequencies are different [10]. Such inter-harmonics generate torque pulsations which, if close to the mechanical torsional natural frequencies (TNF's) of the shaft line, can lead to accelerated mechanical fatigue, lifetime reduction, gear-box damage and system failures [5], [10], [11]. The grid-side inter-harmonic components can also excite the TNF's of turbine-generator groups connected to the same weak network [10]. A possible way to cope with the problem is to move inter-harmonic frequencies away from TNF's by acting on LCI firing angles [5]. Otherwise, the inter-harmonic pollution can be reduced by modifying the converter structure. In [10], it is shown that an interconnection of dc-links can be beneficial for this purpose.

The employment of an LCI drive configuration with interconnected dc-links, however, can have some important drawbacks in regard to the voltage stress imposed on the WFSM stator windings. This problem has never been investigated in the literature so far to the best of authors' knowledge. The issue is considered in this paper, showing that the mentioned topology results in a high voltage to appear between phases belonging to different stator three-phase sets. A noticeable increase is also observed in the voltage between the isolated star points of the two winding sets as a consequence of dc-link interconnection. These phenomena should be taken into careful account in the WFSM design because the winding sets may have coils placed in the same slot and the insulation between such coils must be dimensioned to withstand the relevant voltage stress.

The problem for the designer is therefore to predict the amplitude of the voltage expected to appear between all motor phases and between the two star points (assuming star-connected phases). Such voltages are strongly distorted and change from one working point to the other as they depend upon several parameters such as the ac-grid frequency, the motor frequency, the firing angle of both line-side and motor-side thyristor bridges. Theoretically, to predict motor voltage stresses one should run numerical dynamic simulations of the entire drive system model in all its possible operating conditions. This would be very time-consuming due to the huge number of combinations to be investigated and to the computational burden of each simulation [12], [13].

An alternative approach is proposed in this paper based on a computationally-efficient algorithm to study the LCI-fed WFSM drive steady-state operation with no need for numerically integrating any differential equation. The proposed method results from a circuit analysis of the system and yields a set of purely algebraic equations that can be solved in a closed form. The circuit analysis is performed taking into account the commutation phenomena through appropriate switching functions [14].

The method can be used to almost instantaneously sweep a wide variety of drive operating conditions finding the waveform (and therefore the amplitude) of the voltage between any pair of motor phases for each working scenario as well as the voltage between the star points of the two winding sets. This enables the designer to identify the worst-case condition needed to size the motor insulation system. A further merit of the presented approach over conventional dynamic simulations is that it requires a very limited number of system parameters, which are often difficult to obtain.

The method can be applied to all the drive operating modes characterized by a continuous dc-link current flow. Discontinuous (or pulsed) dc-link current operating modes, which can be adopted during start-up at very low speeds [15], are not covered.

The presented methodology is assessed by comparison with measurements on a real drive system. A good agreement is found between theoretical and experimental results in all the working points taken into account.

The paper is organized as follows. Section II briefly describes the dual-three-phase WFSM drive system under study and defines the voltage-stress issues in its configuration with interconnected dc-links. The proposed algebraic model to investigate these issues is presented in Section III and Section IV, which respectively address the computation of the motor line-to-line voltages and the computation of the voltage between star points. In Section V the method is validated against measurement on a real drive and some examples are provided of how the method can be applied to motor winding insulation sizing.

II. System Description and Problem Statement

Fig. 1 represents a schematic of a dual-three-phase LCI-fed WFSM. The WFSM is equipped with two three-phase windings sets ($a1$, $b1$, $c1$ and $a2$, $b2$, $c2$, respectively) displaced by 30 electrical degrees apart and the two windings are supplied by distinct LCI's (LCI1 and LCI2). The two winding sets are assumed to be star connected to avoid third-harmonic current circulation phenomena and the two star points $n1$ and $n2$ are assumed to be isolated.

The line-side section of the converter is composed of two thyristor rectifiers (REC1 and REC2, Fig. 2). The two main drive arrangements of practical interest are shown in Fig. 2. The most common configuration (see Fig. 2(a)) features totally independent converters with decoupled dc-links; the alternative solution shown in Fig. 2(b) is characterized by an interconnection of the dc-links.

The drive arrangement with interconnected dc-links has been proposed [10] in order to reduce the dc-link current and torque
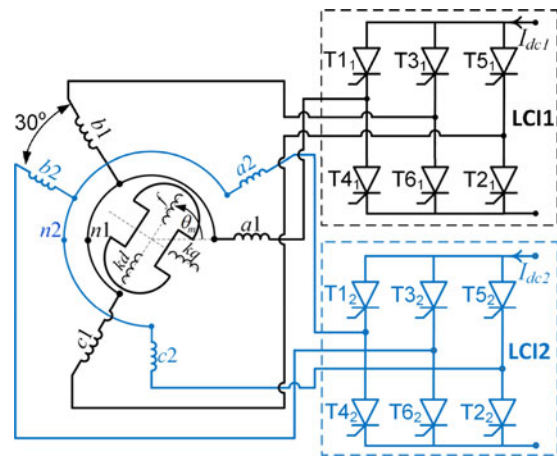

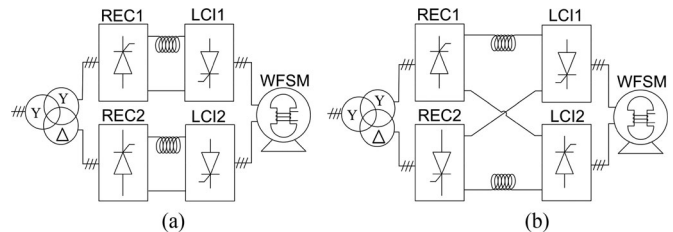Fig. 1. Circuit diagram of LCI-fed dual-three-phase WFSM.

Fig. 2. Possible drive system arrangements: (a) with independent converters; (b) with cross-connected dc-links.
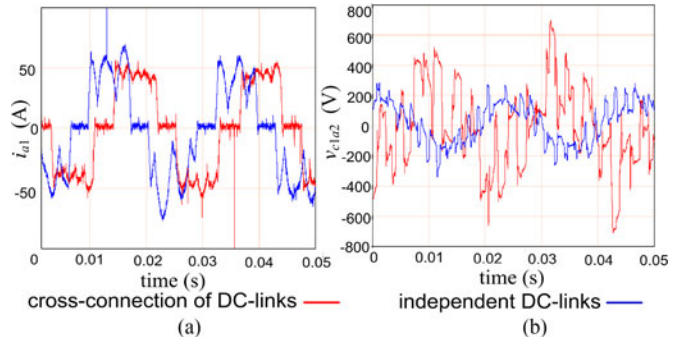

Fig. 3. Recorded waveforms (for the two drive configurations shown in Fig. 2) of: (a) currents in phase $a1$; (b) voltages between phase $c1$ and $a2$.

ripple especially in respect to the inter-harmonic components. However, some experimental comparative observations conducted on the two configurations have highlighted that the interconnected dc-link arrangement suffers from some possible drawbacks due to a much higher voltage stress between phases belonging to different WFSM winding sets. An experimental evidence of this is provided in Fig. 3, which shows the phase currents and voltages between phases $c1$ and $a2$ for the two drive configurations depicted in Fig. 2. The two configurations are implemented with the same equipment (described in Appendix A) by only changing the dc-link connections. The waveforms have been recorded in the same operating conditions shown in Table I.

It is evident from Fig. 3 that, despite a noticeable reduction in the dc-link current ripple due to inter-harmonic mitigation,

TABLE I
OPERATING POINTS FOR THE MEASUREMENTS IN FIG. 3

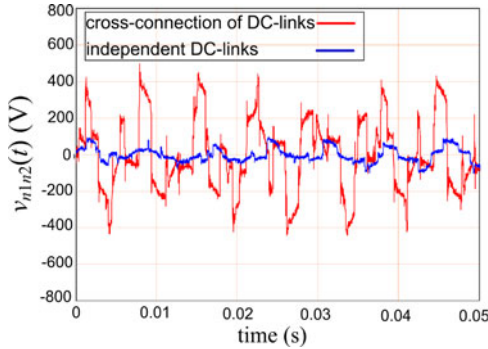|	Independent dc-links	Interconnected dc-links
Speed	1325 r/min	1333 r/min
Mean dc-link current	43 A	43 A
LCI firing angle	130°	128°
Field current	1.70 A	1.77 A

Fig. 4. Recorded waveforms (for the two drive configurations shown in Fig. 2) of the voltage between the two motor star points n1 and n2.

Fig. 5. Interconnected dc-link drive configuration with a simplified motor model.

Fig. 6. Motor line-to-line and phase voltages v_{a1c1}, e_{a1} and motor current i_{a1} with the relevant shifts in electrical radians.

the dc-link interconnection leads to a strong increase in the line-to-line voltage peak between phases $c1$ and $a2$ which belong to different machine winding sets. This can represent a possible concern since, in usual dual-layer short-pitch windings, the coil sides of phases $c1$ and $a2$ can be placed in the same slot, resulting in a remarkable voltage stress across the insulation wall. Similarly, a significant increase can be observed in the voltage recorded between motor star points $n1$ and $n2$ when the dc-links are interconnected, as shown in Fig. 4.

An accurate prediction of the voltage waveforms for the interconnected dc-link configuration is therefore essential for an appropriate sizing of the WFSM winding insulation. Of course, such waveforms could be obtained through a numerical dynamic simulation [12], which should be, however, repeated for all the possible operating conditions to identify the worst-case scenario. This would lead to a huge computational burden due to the large number of time-consuming numerical dynamic simulations required.

To cope with the problem, a computationally-efficient algebraic algorithm to predict machine voltages in arbitrary steady-state operating conditions is developed next.

III. ALGEBRAIC ALGORITHM DERIVATION FOR PREDICTING LINE-TO-LINE VOLTAGES

In this section, the prediction of line-to-line voltages between phases which belong to different WFSM winding sets is addressed.

A. System Modeling and Assumptions

We shall refer to the simplified system configuration shown in Fig. 5, where $u1$, $v1$, $w1$ and $u2$, $v2$, $w2$ are the grid-side voltages that respectively supply the rectifiers REC1 and REC2,
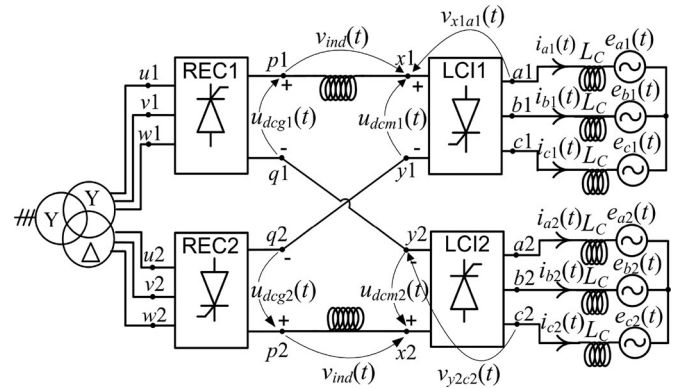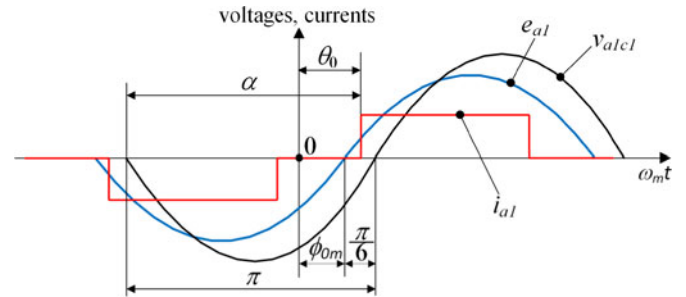
L_C is the commutation inductance [16] and

$$
\begin{aligned}
e_{a1}(t) &= E_m \sin(\omega_m t - \phi_{0m}), \\
e_{b1}(t) &= E_m \sin(\omega_m t - \tfrac{2\pi}{3} - \phi_{0m}) \\
e_{c1}(t) &= E_m \sin(\omega_m t - \tfrac{4\pi}{3} - \phi_{0m}) \\
e_{a2}(t) &= E_m \sin(\omega_m t - \tfrac{\pi}{6} - \phi_{0m}) \\
e_{b2}(t) &= E_m \sin(\omega_m t - \tfrac{\pi}{6} - \tfrac{2\pi}{3} - \phi_{0m}) \\
e_{c2}(t) &= E_m \sin(\omega_m t - \tfrac{\pi}{6} - \tfrac{4\pi}{3} - \phi_{0m}).
\end{aligned} \tag{1}
$$

are the motor back EMF's at electrical speed ω_m. Motor current and voltage waveforms (disregarding commutation notches) are shown in Fig. 6 with the relevant phase shifts.

In particular, α denotes the firing angle (applied to both LCI1 and LCI2) and θ_0 identifies the instant at which the current i_{a1} becomes positive, i.e., the instant at which thyristor $T1_1$ (see Fig. 1) starts conducting. From Fig. 6 one can easily see that

$$
\theta_0 = \phi_{0m} + \tfrac{\pi}{6} - \pi + \alpha = \phi_{0m} - \tfrac{5\pi}{6} + \alpha, \tag{2}
$$

so θ_0 depends on the initial phase of motor back EMF's given in (1) and on the firing angle at which LCI1 and LCI2 are operated.

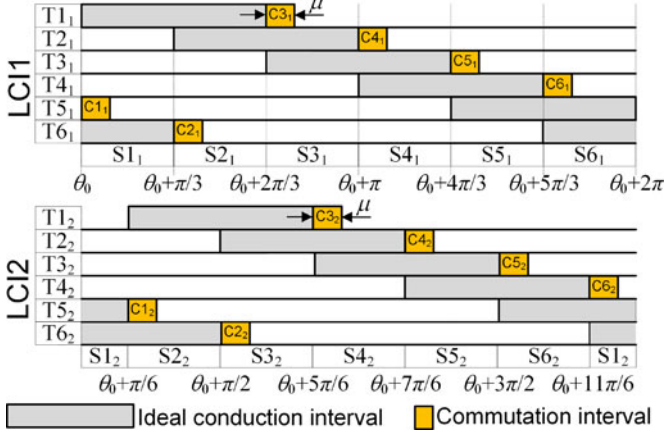Regarding the grid-side section, the following phase voltage expressions are assumed at REC1 and REC2 input terminals,

Fig. 7. Switching pattern for LCI1. The switching pattern for LCI2 is the same shifted by $\pi/6$.

characterized by the electrical frequency ω_g,

$$
\begin{aligned}
v_{u1}(t) &= V_g \sin(\omega_g t - \phi_{0g}), \\
v_{v1}(t) &= V_g \sin(\omega_g t - \tfrac{2\pi}{3} - \phi_{0g}) \\
v_{w1}(t) &= V_g \sin(\omega_g t - \tfrac{4\pi}{3} - \phi_{0g}) \\
v_{u2}(t) &= V_g \sin(\omega_g t - \tfrac{\pi}{6} - \phi_{0g}) \\
v_{v2}(t) &= V_g \sin(\omega_g t - \tfrac{\pi}{6} - \tfrac{2\pi}{3} - \phi_{0g}) \\
v_{w2}(t) &= V_g \sin(\omega_g t - \tfrac{\pi}{6} - \tfrac{4\pi}{3} - \phi_{0g}).
\end{aligned}
\tag{3}
$$

Finally, $x1$, $y1$ and $x2$, $y2$ are used in Fig. 5 to indicate the input dc terminals of LCI1 and LCI2 respectively; similarly, $p1$, $q1$ and $p2$, $q2$ are the output dc terminals of REC1 and REC2.

In the schematic shown in Fig. 5, only commutation inductances are displayed for clarity but in the following mutual inductances between phases will be properly taken into account as well.

In the following of the paper, it will be assumed that:
1) the commutations in the three LCI legs are shifted by $2\pi/(3\omega_m)$ apart according to the switching pattern shown in Fig. 7, where μ indicates the commutation interval in electrical radians and θ_0 is the same as illustrated in Fig. 6;
2) the commutations in LCI2 occur according to the same switching pattern as in LCI1 but shifted by $\pi/(6\omega_m)$, as shown in Fig. 7; similarly, commutations in REC1 and REC2 are shifted by $\pi/(6\omega_g)$.

As a consequence of these assumptions combined with (1)–(3), we have that: the terminal voltage waveforms (including commutation notches) for motor phases in the same winding sets are shifted by $2\pi/(3\omega_m)$; terminal voltage waveforms for homonymous phases belonging to different winding sets (e.g., $a1$ and $a2$) are shifted by $\pi/(6\omega_m)$. The same applies to the grid side with ω_g instead of ω_m.

Finally, dc-link currents feeding both LCI1 and LCI2 are assumed constant and equal to I_{dc} (the two dc-links are series-connected as shown in Fig. 5).

B. General Approach to Algorithm Derivation

The derivation of the proposed algorithm moves from observing that all the line-to-line voltages between a generic pair of motor phases can be found by means of Kirchhoff Voltage Law (KVL), once the voltages $v_{x1a1}(t)$, $v_{p1u1}(t)$ are known. For example, taking phase $c1$ in the first winding set and phase $a2$ in the second one as an example, the voltage between such phases can be expressed as:

$$
v_{c1a2}(t) = -v_{x1c1}(t) + v_{\text{ind}}(t) + u_{\text{dcg1}}(t) + v_{y2a2}(t) \tag{4}
$$

where: v_{ind} is the voltage across the dc-link inductor; u_{dcg1} is the output voltage of REC1; v_{y2a2}, v_{x1c1} are the voltages between phase $a2$ and terminal $y2$ and between phase $c1$ and terminal $x1$, respectively.

In Appendix B it is demonstrated how all the terms which appear in the right-hand side of (4) can be expressed as functions of $v_{x1a1}(t)$ and $v_{p1u1}(t)$.

As a consequence, the problem of computing line-to-line voltages between motor phase pairs is reduced to the computation of the two functions $v_{x1a1}(t)$, $v_{p1u1}(t)$. In the following we shall discuss the detailed computation of $v_{x1a1}(t)$ since $v_{p1u1}(t)$ can be determined with an identical procedure applied to the grid-side section of the drive system.

The function $v_{x1a1}(t)$ will be computed by steps as:

$$
v_{x1a1}(t) = v_{x1a1}^0(t) + \Delta v_{x1a1}^L(t) + \Delta v_{x1a1}^M(t) \tag{5}
$$

where: $v_{x1a1}^0(t)$ is the ideal voltage disregarding commutation effects; $\Delta v_{x1a1}^L(t)$ is a correction term used to take into account voltage drops across commutation inductances L_C (see Fig. 5); $\Delta v_{x1a1}^M(t)$ is a correction term used to take into account the effect of mutual inductances between motor phases.

In the following sections, the computation of the individual terms $v_{x1a1}^0(t)$, $\Delta v_{x1a1}^L(t)$, $\Delta v_{x1a1}^M(t)$ is discussed.

C. Computation of $v_{x1a1}^0(t)$

With reference to Fig. 7, let us start considering the intervals $S1_1$ and $S2_1$. During such intervals, $T1_1$ is conducting and so

$$
v_{x1a1}^0(t) = 0 \quad \text{for} \quad \omega_m t \in [\theta_0, \theta_0 + 2\pi/3]. \tag{6}
$$

During $S3_1$ and $S4_1$, $T3_1$ is conducting (see Fig. 7) and so

$$
\begin{aligned}
v_{x1a1}^0(t) &= -e_{a1}(t) + e_{b1}(t) = (-1 \quad 0 \quad 0)\, \mathbf{v}_{m1}(t) \\
&\text{for } \omega_m t \in [\theta_0 + 2\pi/3, \theta_0 + 4\pi/3]
\end{aligned}
\tag{7}
$$

where the vector $\mathbf{v}_{m1(t)}$ is defined as:

$$
\mathbf{v}_{m1}(t) = \begin{pmatrix} e_{a1}(t) - e_{b1}(t) \\ e_{b1}(t) - e_{c1}(t) \\ e_{c1}(t) - e_{a1}(t) \end{pmatrix}. \tag{8}
$$

Finally, during $S5_1$ and $S6_1$, $T5_1$ is conducting and so:

$$
\begin{aligned}
v_{x1a1}^0(t) &= -e_{a1}(t) + e_{c1}(t) = (0 \quad 0 \quad 1)\, \mathbf{v}_{m1}(t) \\
&\text{for } \omega_m t \in [\theta_0 + 4\pi/3, \theta_0 + 2\pi].
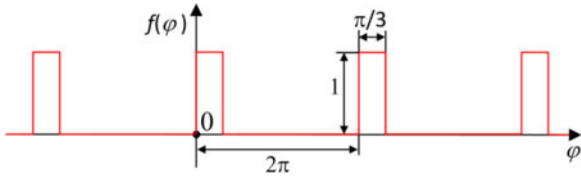\end{aligned}
\tag{9}
$$

4

Fig. 8. Diagram of periodic function $f(\varphi)$.

Equations (6), (7) and (9) can be condensed into the more compact and general form given below:

$$v_{x1a1}^0(t) = \sum_{j=0}^{5} \mathbf{e}_{j+1}^t \mathbf{S}_0 \mathbf{v}_{m1}(t) f\left(\omega_m t - \theta_0 - j\frac{\pi}{3}\right) \quad (10)$$

where: $\mathbf{e}_j$ is the 6×1 column vector having all its elements equal to zero except for the jth element which is equal to one; superscript "t" denotes transposition; $\mathbf{S}_0$ is the constant switching matrix below

$$\mathbf{S}_0 = \begin{pmatrix} 0 & 0 & 0 \\ 0 & 0 & 0 \\ -1 & 0 & 0 \\ -1 & 0 & 0 \\ 0 & 0 & 1 \\ 0 & 0 & 1 \end{pmatrix} \quad (11)$$

and f is the periodic rectangular function plotted in Fig. 8. For the function f the analytical expression below is used:

$$f(\varphi) = \begin{cases} 1 & \text{if } 0 \leq \mathrm{mod}\left(|\varphi| - \frac{\pi}{6}\left[\mathrm{sgn}(\varphi) - 1\right], 2\pi\right) < \frac{\pi}{3} \\ 0 & \text{otherwise} \end{cases} \quad (12)$$

where $\mathrm{mod}(a, b)$ indicates the remainder on dividing a by b and $\mathrm{sgn}(\varphi)$ is equal to 1 if φ is zero or positive, to -1 if φ is negative.

D. Computation of $\Delta v_{x1a1}^L(t)$

This section intends to define the correction term $\Delta v_{x1a1}^L(t)$ which needs to be added to the voltage $v_{x1a1}^0(t)$, computed in Section III-C, in order to account for the voltage drops across commutation inductances L_C (see Fig. 5), while mutual couplings between phases are still disregarded.

The correction term $\Delta v_{x1a1}^L(t)$ is a function that takes non-zero values only during commutation intervals (lasting μ electrical radians each), which are highlighted in Fig. 7 and named Ck_1 with $k = 1, 2, \ldots, 6$. Under the assumption of negligible stator resistance, the commutation angle, μ, can be calculated by the following equation [16]:

$$\mu = \arccos\left[\cos\alpha - \frac{2L_C \omega_m I_{\mathrm{dc}}}{E_m \sqrt{3}}\right] - \alpha. \quad (13)$$

The intervals Ck_1 ($k = 1, 2, \ldots, 6$) will be individually examined next in order to define the function $\Delta v_{x1a1}^L(t)$ inside each of them.

1) Commutation Intervals $C1_1$ and $C2_1$: First of all, let us consider the commutation intervals $C1_1$ and $C2_1$ (see Fig. 7). In the former, the conducting thyristors are $T1_1$, $T5_1$ and $T6_1$, while in the latter the conducting thyristors are $T1_1$, $T2_1$ and $T6_1$. So in both cases, $T1_1$ is conducting and this short circuits
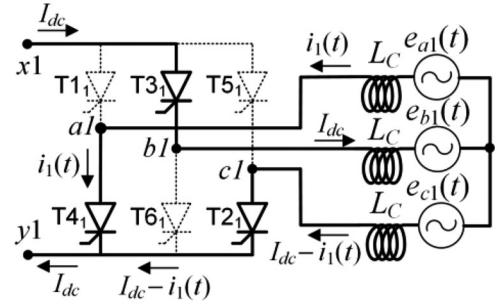

Fig. 9. Equivalent circuit for commutation between $T2_1$ and $T4_1$.

points $a1$ and $x1$, causing the voltage $v_{x1a1}(t)$ to be zero as it can be predicted for $v_{x1a1}^0(t)$ according to (6). Hence there is no correction to apply in commutation intervals $C1_1$ and $C2_1$ and

$$\Delta v_{x1a1}^L(t) = 0$$
$$\text{for } \omega_m t \in [\theta_0, \theta_0 + \mu] \cup [\theta_0 + \frac{\pi}{3}, \theta_0 + \frac{\pi}{3}\mu]. \quad (14)$$

2) Commutation Interval $C3_1$: During this interval, the conducting thyristors are $T1_1$, $T2_1$ and $T3_1$. The conduction of $T1_1$, in particular, causes $v_{x1a1}(t)$ to be zero. However, in the same interval, the voltage $v_{x1a1}^0(t)$ is given by (7). Hence, the correction term can be evaluated as:

$$\Delta v_{x1a1}^L(t) = -v_{x1a1}^0(t) = e_{a1}(t) - e_{b1}(t)$$
$$\text{for } \omega_m t \in \left[\theta_0 + \frac{2\pi}{3}, \theta_0 + \frac{2\pi}{3} + \mu\right] \quad (15)$$

3) Commutation Interval $C4_1$: The conduction paths for LCI1 during $C4_1$ (see Fig. 7) are drawn in Fig. 9 with solid lines. $T2_1$, $T3_1$ and $T4_1$ are conducting. More precisely, the dc-link current I_{dc} is being transferred from phase $c1$ to phase $a1$ through a commutation current $i_1(t)$ which grows from 0 to I_{dc} so that:

$$i_{a1}(t) = -i_1(t), \quad i_{b1}(t) = I_{\mathrm{dc}}, \quad i_{c1}(t) = -I_{\mathrm{dc}} + i_1(t). \quad (16)$$

By applying the KVL to the short-circuit loop in Fig. 9, one can write

$$L_C \, di_{a1}/dt + e_{a1}(t) = L_C \, di_{c1}/dt + e_{c1}(t). \quad (17)$$

By deriving equations in (16) and considering that I_{dc} is constant ($dI_{\mathrm{dc}}/dt = 0$), we find that

$$di_{a1}/dt = -di_{c1}/dt \quad (18)$$

and substituting (18) into (17) we obtain

$$di_{a1}/dt = [e_{c1}(t) - e_{a1}(t)] / (2L_C). \quad (19)$$

Furthermore, from Fig. 9 the voltage $v_{x1a1}(t)$ between terminals $x1$ and $a1$ is demonstrated to be:

$$v_{x1a1}(t) = -e_{a1}(t) + e_{b1}(t) - L_C \, di_{a1}/dt \quad (20)$$

and substituting (19) into (20) gives:

$$v_{x1a1}(t) = e_{b1}(t) - [e_{a1}(t) + e_{c1}(t)] / 2. \quad (21)$$

Now, in the commutation interval $C4_1$ (see Fig. 7), $v_{x1a1}^0(t)$ is given by (7). Therefore, the expression for the correction term

5

can be derived from (7) and (21) as follows:

$$\Delta v^L_{x1a1}(t) = v_{x1a1}(t) - v^0_{x1a1}(t) = [e_{a1}(t) - e_{c1}(t)]/2$$
$$\text{for } \omega_m t \in [\theta_0 + \pi, \theta_0 + \pi + \mu] \tag{22}$$

4) Commutation Intervals C5$_1$ and C6$_1$: With the same reasoning used for the interval C4$_1$, we can obtain the value of $\Delta v^L_{x1a1}(t)$ in the commutation intervals C5$_1$ and C6$_1$ (see Fig. 7). For the sake of brevity, we just give the results:

$$\Delta v^L_{x1a1}(t) = [e_{b1}(t) - e_{c1}(t)]/2$$
$$\text{for } \omega_m t \in \left[\theta_0 + \frac{4\pi}{3}, \theta_0 + \frac{4\pi}{3} + \mu\right] \tag{23}$$

$$\Delta v^L_{x1a1}(t) = [e_{a1}(t) - e_{b1}(t)]/2$$
$$\text{for } \omega_m t \in \left[\theta_0 + \frac{5\pi}{3}, \theta_0 + \frac{5\pi}{3} + \mu\right] \tag{24}$$

5) General Expression: In more compact and general terms, equations (14), (15), (22), (23) and (24) can be condensed into the following:

$$\Delta v^L_{x1a1}(t) = \sum_{j=0}^{5} \mathbf{e}^t_{j+1} \mathbf{S}_L \mathbf{v}_{m1}(t) g\left(\omega_m t - \theta_0 - j\frac{\pi}{3}\right) \tag{25}$$

where the switching matrix $\mathbf{S}_L$ and the rectangular periodic function g are defined as:

$$\mathbf{S}_L = \frac{1}{2} \begin{pmatrix} 0 & 0 & 0 \\ 0 & 0 & 0 \\ 2 & 0 & 0 \\ 0 & 0 & -1 \\ 0 & 1 & 0 \\ 1 & 0 & 0 \end{pmatrix} \tag{26}$$

$$g(\varphi) = \begin{cases} 1 & \text{if } 0 \leq \mathrm{mod}\left(|\varphi| - \frac{\mu}{2}[\mathrm{sgn}(\varphi) - 1], 2\pi\right) < \mu \\ 0 & \text{otherwise.} \end{cases} \tag{27}$$

The diagram of g(φ) is the same as for f(φ) (see Fig. 8) except for the "pulse" duration which is μ instead of $\pi/3$.

E. Computation of $\Delta v^M_{x1a1}(t)$

To complete the modeling procedure, the effect of mutual couplings during commutation transients is investigated in this subsection. In other words, the correction term $\Delta v^M_{x1a1}(t)$ is intended to account for the effect that the commutations taking place in LCI2 have on the voltage $v_{x1a1}(t)$.

In order to determine $\Delta v^M_{x1a1}(t)$ we shall refer to the switching pattern in LCI2 as illustrated in Fig. 7 and we shall consider each of the commutation intervals Ck$_2$ (k = 1, 2, ..., 6) to determine the function $\Delta v^M_{x1a1}(t)$ over it.

1) Commutation Intervals C1$_2$ and C2$_2$: In C1$_2$ the commutation in LCI2 occurs between thyristors T1$_2$ and T5$_2$ starting at $\omega_m t = \theta_0 + \pi/6$ (see Fig. 7). In this period T1$_1$ is conducting and the commutation between T1$_2$ and T5$_2$ does not influence $v_{x1a1}(t)$ which is equal to zero.

Similarly, during the commutation interval C2$_2$ (between T2$_2$ and T6$_2$), T1$_1$ is still conducting and $v_{x1a1}(t)$ continues to be
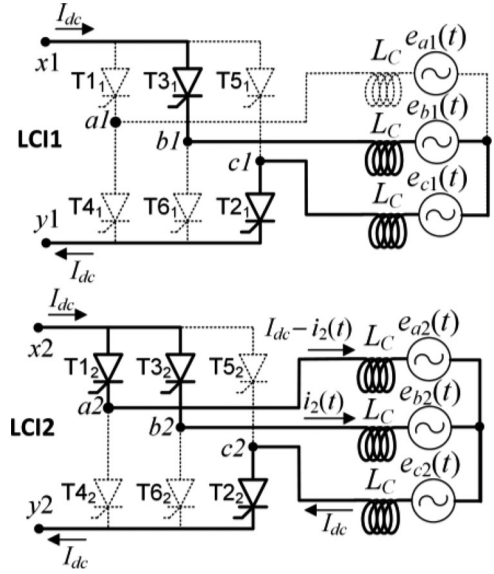

Fig. 10. Equivalent circuits of LCI1 and LCI2 during commutation interval C3$_2$.

zero. So we can write:

$$\Delta v^M_{x1a1}(t) = 0$$
$$\text{for } \omega_m t \in \left[\theta_0 + \frac{\pi}{6}, \theta_0 + \frac{\pi}{6} + \mu\right] \cup \left[\theta_0 + \frac{\pi}{2}, \theta_0 + \frac{\pi}{2} + \mu\right]. \tag{28}$$

2) Commutation Interval C3$_2$: During the commutation interval C3$_2$ (between T1$_2$ and T3$_2$), the situation in LCI1 and LCI2 is shown in Fig. 10. In LCI2 the commutation current $i_2(t)$ flows through phases $a2$ and $b2$ so that:

$$i_{a2}(t) = I_{dc} - i_2(t), \quad i_{b2}(t) = i_2(t), \quad i_{c2}(t) = -I_{dc}. \tag{29}$$

Based on Fig. 10, we can observe that the voltage between points $x1$ and $a1$, without considering mutual couplings, would be simply $e_{b1}(t) - e_{a1}(t)$. To account for mutual coupling effects we must add $\Delta v^M_{x1a1}(t)$:

$$v_{x1a1}(t) = e_{b1}(t) - e_{a1}(t) + \Delta v^M_{x1a1}(t). \tag{30}$$

The correction term $\Delta v^M_{x1a1}(t)$ can be derived as explained in Appendix C in the following form:

$$\Delta v^M_{x1a1}(t) = M_{eq} di_2/dt. \tag{31}$$

In (31) the parameter M_{eq} is given by

$$M_{eq} = 3L^\sigma_{a1,a2} + \frac{\sqrt{3}}{2}\left(L'''_d + L'''_q\right) \tag{32}$$

with $L^\sigma_{a1,a2}$ being the mutual inductance between phases $a1$ and $a2$ due to leakage flux and L'''_d, L'''_q defined as

$$L'''_d = \left(\frac{1}{L_{md}} + \frac{1}{L^\sigma_{kd}} + \frac{1}{L^\sigma_f}\right)^{-1}, L'''_q = \left(\frac{1}{L_{mq}} + \frac{1}{L^\sigma_{kq}}\right)^{-1} \tag{33}$$

where L_{md}, L_{mq}, are the magnetizing inductances along d and q axes and L^σ_{kd}, L^σ_{kq}, L^σ_f are defined in Appendix C.

Finally, from Fig. 10, the KVL applied to the closed loop formed by phases $a2$ and $b2$ gives:

$$di_2/dt = [e_{a2}(t) - e_{b2}(t)]/2L_C. \tag{34}$$

This can be substituted into (31) obtaining:

$$\Delta v_{x1a1}^M(t) = M_{eq}[e_{a2}(t) - e_{b2}(t)]/2L_C$$
$$\text{for } \omega_m t \in \left[\theta_0 + \tfrac{5\pi}{6}, \theta_0 + \tfrac{5\pi}{6} + \mu\right]. \tag{35}$$

3) Commutation Interval $C4_2$: During the interval $C4_2$ (see Fig. 7), the commutation between phases $a2$ and $c2$ takes place in LCI2 while, in LCI1, $T3_1$ is still in conduction state connecting the terminals $b1$ and $x1$ as in the interval $C3_2$. Therefore, during $C4_2$, the same system of differential equations (C1) given in Appendix C can be written provided that $b2$ is replaced by $c2$. By applying the same procedure described in Appendix C for the commutation interval $C3_2$, we can obtain the following expression for $\Delta v_{x1a1}^M(t)$ in $C4_2$:

$$\Delta v_{x1a1}^M(t) = M'_{eq} di'_2/dt \tag{36}$$

where i'_2 is the commutation current between phases $a2$ and $c2$ and the parameter M'_{eq} takes the expression below:

$$M'_{eq} = -L_{b1,a2}^\sigma + L_{b1,c2}^\sigma - L_{a1,c2}^\sigma + L_{a1,a2}^\sigma$$
$$- \left(L_d''' - L_q'''\right)\cos\left(2\theta_r - \tfrac{7\pi}{6}\right). \tag{37}$$

Now we can observe that phases $b1$ and $a2$ are orthogonal as well as phases $a1$ and $c2$. Therefore their mutual leakage inductance is zero [17], i.e.,

$$L_{b1,a2}^\sigma = L_{a1,c2}^\sigma = 0. \tag{38}$$

Furthermore, phases $a1$, $a2$ are displaced by 30 electrical degrees while phases $b1$, $c2$ are displaced by $180 - 30 = 150$ electrical degrees. Hence, their mutual leakage inductances are opposite [17]:

$$L_{a1,a2}^\sigma = -L_{b1,c2}^\sigma. \tag{39}$$

Finally, we can observe that the term $L_d''' - L_q'''$ usually takes a negligible value compared to the commutation inductance L_C. For instance, in the example machine whose parameters are given in Appendix A, it is more than 13 times lower than L_C. Hence, assuming $L_d''' - L_q''' \cong 0$ and based on (38), (39), one can conclude from (37) that:

$$\Delta v_{x1a1}^M(t) \cong 0 \quad \text{for} \quad \omega_m t \in \left[\theta_0 + \tfrac{7\pi}{6}, \theta_0 + \tfrac{7\pi}{6} + \mu\right]. \tag{40}$$

4) Commutation Interval $C5_2$: Following exactly the same reasoning as for $C4_2$, it is possible to prove that also in the commutation interval $C5_2$ the correction term $\Delta v_{x1a1}^M(t)$ accounting for mutual couplings is close to zero, hence:

$$\Delta v_{x1a1}^M(t) \cong 0 \quad \text{for} \quad \omega_m t \in \left[\theta_0 + \tfrac{3\pi}{2}, \theta_0 + \tfrac{3\pi}{2} + \mu\right]. \tag{41}$$

5) Commutation Interval $C6_2$: Finally, following the same reasoning as for $C3_2$ we can prove that during the commutation interval $C6_2$ the correction term $\Delta v_{x1a1}^M(t)$ is given by:

$$\Delta v_{x1a1}^M(t) = M_{eq}[e_{a2}(t) - e_{b2}(t)]/2L_C$$
$$\text{for } \omega_m t \in \left[\theta_0 + \tfrac{11\pi}{6}, \theta_0 + \tfrac{11\pi}{6} + \mu\right]. \tag{42}$$
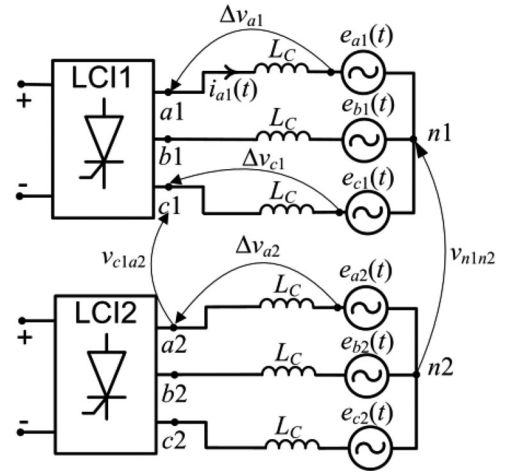

Fig. 11. Circuit model for the determination of the voltage $\Delta v_{n1,n2}$ between the isolated star points $n1$, $n2$ of motor winding sets.

6) General Expression: In more compact and general terms, equations (28), (35), (40)–(42) can be condensed into the following form:

$$\Delta v_{x1a1}^M(t) = \sum_{j=0}^{5} \mathbf{e}_{j+1}^t \mathbf{S}_M \mathbf{v}_{m2}(t) g\left(\omega_m t - \theta_0 - j\tfrac{\pi}{3} - \tfrac{\pi}{6}\right). \tag{43}$$

where g is the periodic rectangular function defined by (27), the switching matrix $\mathbf{S}_M$ and the voltage vector $\mathbf{v}_{m2}$ are given below:

$$\mathbf{S}_M = \frac{M_{eq}}{2L_C}\begin{pmatrix} 0 & 0 & 0 \\ 0 & 0 & 0 \\ 1 & 0 & 0 \\ 0 & 0 & 0 \\ 0 & 0 & 0 \\ 1 & 0 & 0 \end{pmatrix}, \mathbf{v}_{m2}(t) = \begin{pmatrix} e_{a2}(t) - e_{b2}(t) \\ e_{b2}(t) - e_{c2}(t) \\ e_{c2}(t) - e_{a2}(t) \end{pmatrix}. \tag{44}$$

IV. Algebraic Algorithm Derivation for Predicting the Voltage Between Motor Star Points

As mentioned in Section II, the dc-link interconnection according to the LCI drive topology shown in Fig. 2(b) leads to a noticeable increase in the voltage between motor phases belonging to different winding sets (see Fig. 3(b)) as well as between the star points of the two winding sets (see Fig. 4). An algebraic approach to the prediction of line-to-line voltage in the crossed-dc-link drive topology has been presented in Section III. Hereinafter, the same approach is extended to the calculation of the voltage between motor star points $n1$, $n2$.

For the purpose of the study, let us consider the circuit model shown in Fig. 11. In order to determine $v_{n1n2}(t)$, by applying the KVL to the circuit shown in Fig. 11 we obtain:

$$v_{n1n2}(t) = e_{a2}(t) + \Delta v_{a2}(t) + v_{c1a2}(t) - \Delta v_{c1}(t) - e_{c1}(t) \tag{45}$$

where Δv_{a2} and Δv_{c1} denote the voltage drops across commutation inductances.

In (45), the voltage $v_{c1a2}(t)$ between phase terminals $c1$ and $a2$ belonging to different winding sets is derived as explained in Section III; voltages $e_{c1}(t), e_{a2}(t)$ are the machine back EMF's and are known quantities from (1); the only unknowns are therefore the voltage drops $\Delta v_{c1}, \Delta v_{a2}$ across commutation inductances. These two terms can be also obtained through the switching function approach developed in Section III. As an example, the procedure to compute the voltage drop Δv_{a1} (see Fig. 11) will be detailed in the following: once Δv_{a1} is known, Δv_{c1} and Δv_{a2} (as well as the voltage drops across all the other phase commutation inductances) can be obtained by appropriate phase shifts as discussed in Sections II-A.

Similar to $v_{x1a1}(t), \Delta v_{a1}(t)$ is affected by the commutations in both LCI1 and LCI2. Therefore, we can write

$$\Delta v_{a1}(t) = \Delta v_{a1}^L(t) + \Delta v_{a1}^M(t), \tag{46}$$

where, Δv_{a1}^L is the component due to the commutations in LCI1 and Δv_{a1}^M is the component due to the commutations in LCI2.

A. Computation of $\Delta v_{a1}^L(t)$

The term $\Delta v_{a1}^L(t)$ can be written as follows:

$$\Delta v_{a1}^L(t) = L_C \, di_{a1}/dt. \tag{47}$$

Assuming a smooth dc-link current as in the rest of the paper, $\Delta v_{a1}^L(t)$ takes a non-zero value during the commutations in which either thyristor $T1_1$ or thyristor $T4_1$ is conducting. In other words, $\Delta v_{a1}^L(t)$ is non-zero during $C1_1, C3_1, C4_1, C6_1$ (see Fig. 7) and zero during $C2_1, C5_1$ (see Fig. 7). Taking interval $C4_1$ as an example, (19) and (47) show that $\Delta v_{a1}^L(t)$ is equal to $[e_{c1}(t) - e_{a1}(t)]/2$. The expression for $\Delta v_{a1}^L(t)$ in the other commutation intervals, Ck_1, can be deduced according to the explanations given in Section III-D. As a result, the following final and compact expression for $\Delta v_{a1}^L(t)$ is obtained:

$$\Delta v_{a1}^L(t) = \sum_{j=0}^{5} \mathbf{e}_{j+1}^t \mathbf{S}_L' \mathbf{v}_{m1}(t) g\left(\omega_m t - \theta_0 - j\tfrac{\pi}{3}\right) \tag{48}$$

where

$$\mathbf{S}_L' = \frac{1}{2}\begin{pmatrix} 0 & 0 & 1 \\ 0 & 0 & 0 \\ -1 & 0 & 0 \\ 0 & 0 & 1 \\ 0 & 0 & 0 \\ -1 & 0 & 0 \end{pmatrix}. \tag{49}$$

B. Computation of $\Delta v_{a1}^M(t)$

As regards the term $\Delta v_{a1}^M(t)$ in (46), it accounts for the effect of the commutations occurring in LCI2 during the generic intervals Ck_2. Mathematically, we can write:

$$\Delta v_{a1}^M(t) = M_{\mathrm{eq},a1} \, di_2/dt \tag{50}$$

where i_2 is the commutation current flowing through the pair of commutating phases in LCI2 and $M_{\mathrm{eq},a1}$ is the mutual inductance between the loop formed by this pair of phases and phase $a1$. The expression of $M_{\mathrm{eq},a1}$ actually changes depending on the commutation interval Ck_2 being taken into account. The

approach to determine $M_{\mathrm{eq},a1}$ in each of the intervals Ck_2 is the same followed in Appendix C as it considers the system of differential equation governing machine transients during Ck_2. The procedure is briefly recalled in the following subsections to justify the results.

1) Commutation Intervals $C3_2$ and $C6_2$: In Appendix C, the commutation interval $C3_2$ is investigated, where $a2$ and $b2$ commutate in LCI2. Based on the system of differential equations governing the machine transient, it is found that, during $C3_2$, the mutual inductance $M_{\mathrm{eq},a1}$ takes the expression given in (C6). The same expression also holds for the commutation interval $C6_2$, in which the same phases $a2$ and $b2$ commutate.

2) Commutation Intervals $C1_2$ and $C4_2$: During $C1_2$ and $C4_2$ the commutating phases in LCI2 are $a2$ and $c2$. So the system of differential equations (C1) applies provided that subscript $b2$ is replaced by $c2$ and considering $di_{a2}/dt = -di_{c2}/dt = di_2/dt$. Its solution yields the following expression for $M_{\mathrm{eq},a1}$:

$$M_{\mathrm{eq},a1} = \left(L_{a1,a2}^\sigma - L_{a1,c2}^\sigma\right) + \sqrt{3}\left(L_d''' + L_q'''\right)/6$$
$$+ \sqrt{3}\left(L_d''' - L_q'''\right)\sin\left(2\theta + \pi/6\right)/3$$
$$\text{for } \omega_m t \in \left[\theta_0 + \tfrac{\pi}{6}, \theta_0 + \tfrac{\pi}{6} + \mu\right] \cup \left[\theta_0 + \tfrac{7\pi}{6}, \theta_0 + \tfrac{7\pi}{6} + \mu\right]. \tag{51}$$

3) Commutation Intervals $C2_2$ and $C5_2$: During $C2_2$ and $C5_2$, the commutating phases in LCI2 are $b2$ and $c2$. So the system of differential equations (C1) applies provided that subscript $a2$ is replaced by $c2$ and considering $di_{c2}/dt = -di_{b2}/dt = di_2/dt$. Its solution yields the following expression for $M_{\mathrm{eq},a1}$:

$$M_{\mathrm{eq},a1} = \left(-L_{a1,b2}^\sigma + L_{a1,c2}^\sigma\right) + \sqrt{3}\left(L_d''' + L_q'''\right)/6$$
$$- \sqrt{3}\left(L_d''' - L_q'''\right)\sin\left(2\theta - \pi/6\right)/3$$
$$\text{for } \omega_m t \in \left[\theta_0 + \tfrac{\pi}{2}, \theta_0 + \tfrac{\pi}{2} + \mu\right] \cup \left[\theta_0 + \tfrac{3\pi}{2}, \theta_0 + \tfrac{3\pi}{2} + \mu\right]. \tag{52}$$

4) General Expression: As already observed in Appendix C, the expressions (C6), (51), (52) found for $M_{\mathrm{eq},a1}$ can be simplified observing that the term $L_d''' - L_q'''$ is usually much smaller than $L_d''' + L_q'''$. This enables us to simplify the formula for $E_{\mathrm{eq},a1}$ by removing the dependency on the rotor position; furthermore, the mutual leakage inductances in (C6), (51), (52) can be written as functions of the only leakage inductance parameter $L_{a1,a2}^\sigma$ according to (C9). As a result, $M_{\mathrm{eq},a1}$ can be approximated as follows:

$$M_{\mathrm{eq},a1} = \begin{cases} M_{\mathrm{eq}}/3 & \text{during } C1_2 \text{ and } C4_2 \\ M_{\mathrm{eq}}/3 & \text{during } C2_2 \text{ and } C5_2 \\ -2M_{\mathrm{eq}}/3 & \text{during } C3_2 \text{ and } C6_2 \end{cases} \tag{53}$$

where M_{eq} is the inductance parameter defined by (32).

Finally, the derivative di_2/dt in (50) can be easily expressed as a function of motor EMF's e_{a2}, e_{b2}, e_{c2} as already done in (34) based on the KVL applied to the pair of commutating phases in LCI2. This gives:

$$di_2/dt = \frac{1}{2L_C}\begin{cases} e_{c2}(t) - e_{a2}(t) & \text{during } C1_2 \text{ and } C4_2 \\ e_{b2}(t) - e_{c2}(t) & \text{during } C2_2 \text{ and } C5_2 \\ e_{a2}(t) - e_{b2}(t) & \text{during } C3_2 \text{ and } C6_2 \end{cases}. \tag{54}$$
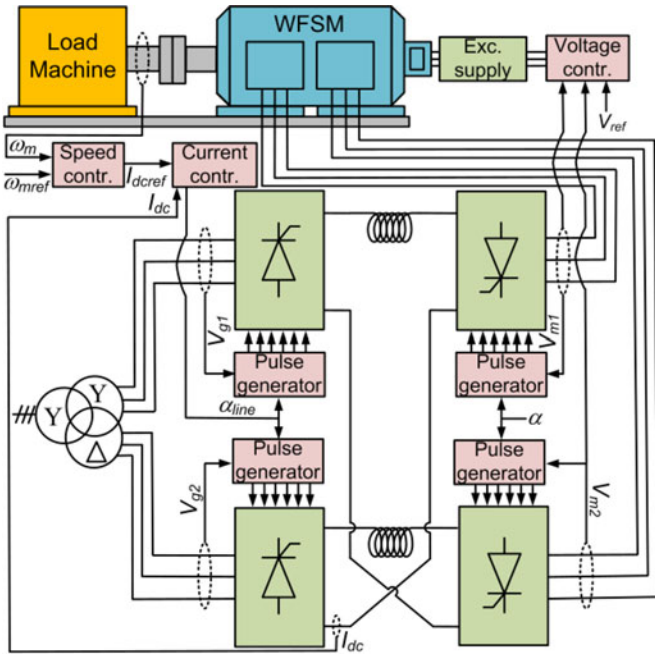
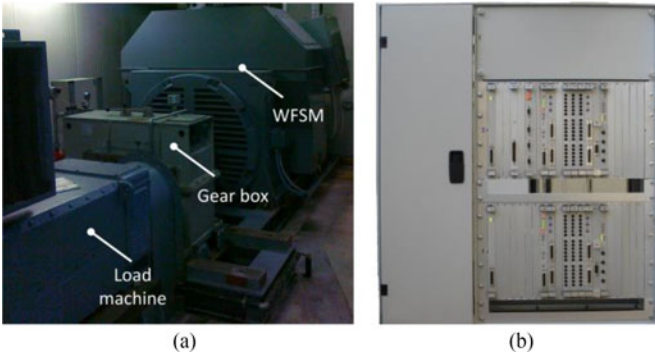Fig. 12. Schematic of the overall drive arrangement used for testing.

Fig. 13. Pictures of the testing equipment: (a) WFSM and load, (b) control system and converter cubicle.

TABLE II
OPERATING POINTS FOR THE MEASUREMENTS

Operating point A		Operating point B	
Motor speed	890 r/min	Motor speed	1150 r/min
α	125°	α	155°
α_{line}	66°	α_{line}	55°
$V_{m1} = V_{m2}^a$	270 V	$V_{m1} = V_{m2}^a$	270 V
$V_{g1} = V_{g2}^a$	460 V	$V_{g1} = V_{g2}^a$	460 V
I_{dc}	43 A	I_{dc}	43 A

^{a} Line-to-line rms voltage.

of the motor winding insulation is provided. In the drive system functional schematic depicted in Fig. 12, the motor electrical speed ω_m is adjusted to follow the reference $\omega_{m\,\text{ref}}$ with a closed-loop control acting on the dc-link current I_{dc}. This in turn is controlled with a current regulation loop acting on the rectifier firing angle α_{line}. Conversely, the LCI firing angle α is maintained constant in a given operating point. Finally, the motor terminal voltages (V_{m1}, V_{m2}) are adjusted to follow the reference V_{ref} by acting on the motor excitation.

The two LCI's included in the drive used as a test bench have cross-connected dc-links as drawn in Fig. 2(b). The ratings and significant parameters of the WFSM required for the algebraic model implementation are provided in Appendix A.

A. Experimental Validation of Line-to-Line Voltage Waveform Prediction

This section is dedicated to experimentally assessing the ability of the algebraic method presented in Section III to predict the motor line-to-line voltage waveforms during drive steady-state operation. For this purpose, the test drive (see Figs. 12–13, Appendix A) is operated in a variety of working conditions and, in each of them, measurements are compared to the algebraic model results. As an example, the two operating points detailed in Table II are next taken into account for detailed validation purposes.

Some results, referring to operating point A, are provided in Fig. 14, while Fig. 15 refers to operating condition B.

First of all, Fig. 14(a) shows the line-to-line voltage between two phases ($a1$, $c1$) of the same motor three-phase set and between two phases ($u1$, $w1$) in the same transformer secondary winding. It can be seen that, in both cases, the voltage waveforms are close to the sinusoidal shape except for the commutation notches. Hence, for this kind of voltages, there is no need for a dedicated calculation algorithm to predict their peak value. However, the proposed methodology is applied to predict the v_{a1c1} voltage obtaining a satisfactory matching as it can be seen from Fig. 14(a).

In Fig. 14(b) and (c), the focus is moved onto the voltage between phases ($c1$, $a2$) belonging to different motor three-phase sets. These figures clearly show how such voltages are extremely distorted and far from a sinusoidal pattern, which justifies the use of a dedicated calculation algorithm to predict their peak amplitudes.

Fig. 14(b) and (c) illustrate the comparison between the measured voltage and the waveforms obtained with the proposed

Substitution of (53) and (54) into (50) leads to the final compact expression below:

$$\Delta v_{a1}^M(t) = \sum_{j=0}^{5} \mathbf{e}_{j+1}^t \mathbf{S}_M' \mathbf{v}_{m2}(t) g\left(\omega_m t - \theta_0 - j\frac{\pi}{3} - \frac{\pi}{6}\right) \tag{55}$$

with the switching matrix $\mathbf{S}_M'$ defined as:

$$\mathbf{S}_M' = \frac{M_{\text{eq}}}{3 \times 2L_C} \begin{pmatrix} 0 & 0 & 1 \\ 0 & 1 & 0 \\ -2 & 0 & 0 \\ 0 & 0 & 1 \\ 0 & 1 & 0 \\ -2 & 0 & 0 \end{pmatrix}. \tag{56}$$

V. EXPERIMENTAL VALIDATION AND APPLICATION EXAMPLE

In this Section, the algebraic model discussed in the paper is validated against measurements on the test drive system shown in Figs. 12 and 13 and an application example to the sizing
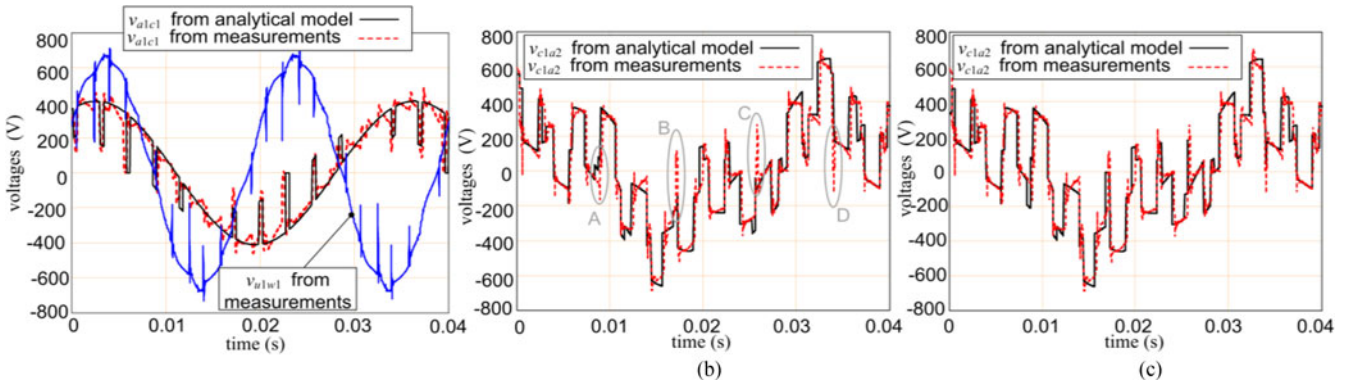
Fig. 14. Comparison between measurement and analytical model results in operating point A for: (a) v_{a1c1}; (b) v_{c1a2} disregarding mutual couplings between three-phase sets; (c) v_{c1a2} taking mutual couplings into account.
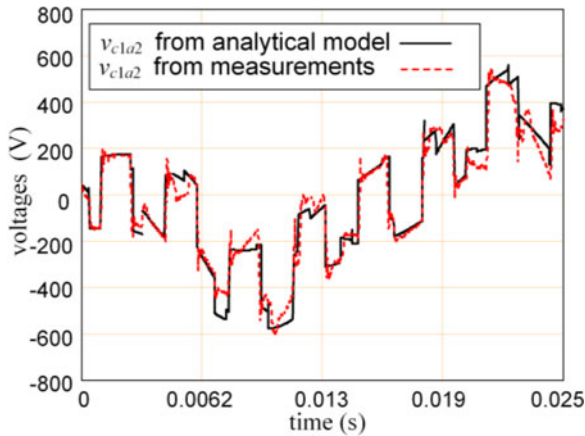

Fig. 15. Comparison between measurement and analytical model results in operating point B for the voltage between phase terminals $c1$ and $a2$.
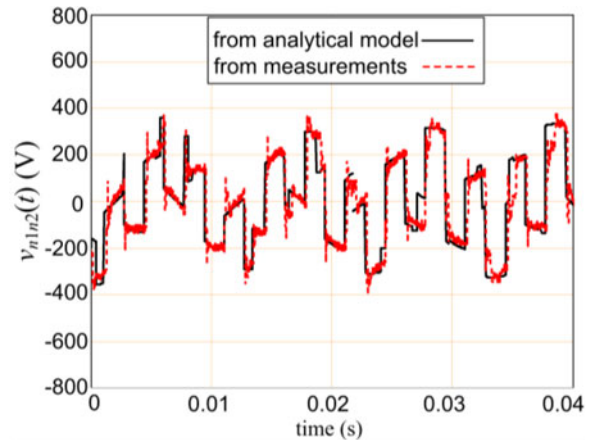

Fig. 16. Comparison between measurement and analytical model results in operating point A for the voltage between isolated star points $n1$ and $n2$.

algorithm in its two different versions, respectively: in Fig. 14(b) an algorithm version is used where only commutation inductances are taken into account and mutual couplings between motor three-phase sets are disregarded, according to what has been explained in Section III-D. Conversely, in Fig. 14(c), the algorithm version including mutual couplings (Section III-E) is adopted. It can be seen that the matching is quite satisfactory for both algorithm versions, although the less accurate one fails to reproduce some voltage peaks, marked with letters A, B, C, D in Fig. 14(b).

A further satisfactory validation of the complete algebraic model is given in Fig. 15, which refers to operating point B (see Table II).

As final remark it can be noted that at some points (e.g., around instants $t = 0.03$ s in the recordings given in Fig. 14(b) and (c)), a discrepancy arises between measurements and simulation results in terms of voltage slope. This is due to the dc-link current ripple and, more precisely, to the voltage drop it generates across the resistance and inductance of the relatively long cables connecting the inverter to the machine. In fact, current ripples exist in the real drive system while they are disregarded in the modelling procedure as specified in Section III-A. The mentioned discrepancies, however, do not invalidate the

proposed analytical approach as the voltage average values in the time intervals where they occur can be, in any case, satisfactorily predicted as it can be seen from Figs. 14 and 15.

B. Experimental Validation for Voltage Waveform Prediction Between Isolated Star Points

This section is dedicated to experimentally assessing the ability of the algebraic method presented in Section IV to predict the voltage between the isolated star points of the two motor winding sets during drive steady-state operation.

For the purpose of an experimental assessment, recordings are collected on the test drive (see Figs. 12–13, Appendix A) during its operation in the working point A detailed in Table II. The comparison between the measurement and the analytical prediction for the voltage between motor isolated star points $n1$ and $n2$ (see Fig. 1) is given in Fig. 16, showing a satisfactory agreement.

C. Application Example to Motor Winding Dimensioning

In this subsection, an application example is given of how the proposed method can be used to properly size the motor winding insulation for the dual-LCI drive arrangement under
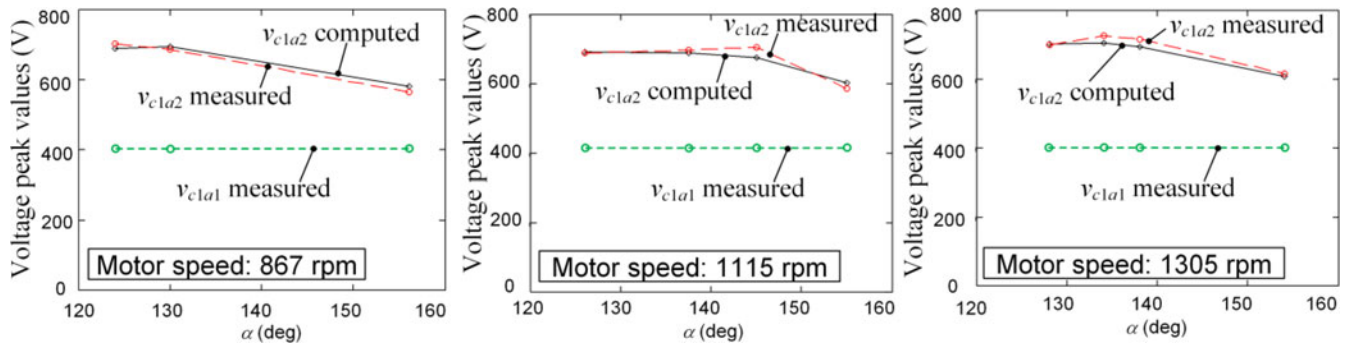
Fig. 17. Peak values of voltage v_{c1a2} (from measurement and computation) and v_{c1a1} as a function of firing angle α for different motor speeds. In the three operating points the dc-link current is constant and equal to 43 A.

study. For this purpose, the proposed algebraic algorithm is run for a large number of operating points in order to determine the highest voltage peak associated to each of them. In fact, for each operating point, a voltage waveform like those shown in Figs. 14–15 can be found and the maximum of the voltage can be extracted. Example results of this procedure are shown in Fig. 17, where the peak value of the voltage v_{c1a2} is plotted against the LCI firing angle α for three different motor speeds, the same terminal voltage v_{c1a1} and the same dc-link current I_{dc}. The computed values are also compared to the measured ones collected on the test drive.

From the diagrams, it is confirmed that the voltage v_{c1a2} between phases in different winding sets has a peak value that is considerably higher than the voltage v_{c1a1} between phases in the same winding set. The use of the proposed algorithm makes it possible to quantify this phenomenon. For example, in the operating point considered in Fig. 14, we have that v_{c1a2} is around 1.8 times v_{a1c1}.

VI. Conclusion

WFSM's with dual-three-phase sets, each fed by an LCI, are widely used in high-power applications. An effective way to reduce inter-harmonic torque ripples in this kind of drives consists of interconnecting the dc-links of the two LCI's. However, it has been shown in this paper how the dc-link interconnection leads to increased voltage amplitudes to appear between motor phases and between the isolated star points of the two three-phase winding sets with respect to the usual arrangement with independent dc-links. This requires a careful sizing of the motor winding insulation. The paper has presented a computationally efficient way to predict motor voltage waveforms at steady state. The proposed algorithm does not involve the solution of any differential equation and uses purely algebraic closed-form equations based on properly-defined switching functions. A further merit is that it requires the knowledge of a very limited set of system parameters. The accuracy of the presented algorithm has been successfully assessed by comparison with measurements taken on a test drive system. As a result, it has been proved to be a very effective tool for the fast and accurate prediction of the voltage stress on the motor winding in steady-state conditions. Such a tool can help designers identify the worst-case scenario to safely size the insulation system of the motor windings.

TABLE III
WFSM Ratings

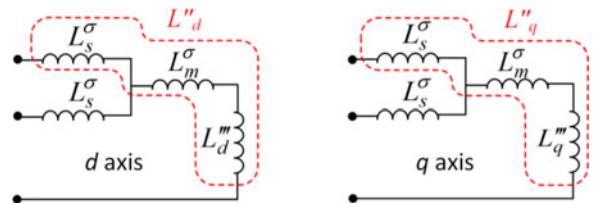| Rated power	250 kW	Rated power factor	0.9
Line-to-line voltage	380 V	Speed	1500 r/min
Stator phase current	225 A	Number of poles	4

Fig. 18. d-axis and q-axis equivalent circuits of the dual-three-phase WFSM including only inductive elements and with shorted field winding.

TABLE IV
WFSM Parameters Used in the Analytical Model

L_s^σ	9.6×10^{-2} mH	L_d''	2.5×10^{-1} mH
L_m^σ	1.5×10^{-2} mH	L_q''	2.7×10^{-1} mH

Appendix A

The ratings of the WFSM used for testing are given in Table III.

For the purpose of the paper, the parameters needed to fully define the algebraic model being set forth are: the commutation inductance $L_C = \left(L_d'' + L_q'' \right)/2$[6], [16]; the inductances L_d''', L_q''' defined by (33) as well as the leakage inductance $L_{a1,a2}^\sigma$, which appear in (32).

All these parameters can be computed based on the WFSM d-axis and q-axis equivalent circuits depicted in Fig. 18, where only inductive elements (whose values are given in Table IV) are shown since they are of interest for the paper.

In particular, the parameters L_d''' and L_q''' are related to the d-axis and q-axis sub-transient inductances L_d'', L_q'' through the following relationships:

$$L_d''' = L_d'' - \left(L_s^\sigma + L_m^\sigma \right), \quad L_q''' = L_q'' - \left(L_s^\sigma + L_m^\sigma \right). \quad \text{(A1)}$$

and the stator leakage inductance $L_{a1,a2}^{\sigma}$ can be computed from L_m^{σ} as explained by the following relationship:

$$L_{a1,a2}^{\sigma} = L_m^{\sigma}/\sqrt{3} \qquad (A2)$$

where L_m^{σ} is the leakage inductance component which appears in the dual-three-phase WFSM equivalent circuit in Park's coordinates (see Fig. 18). The justification of (A2) directly descends from the application of Clark's transform as defined in [18] to the dual-three-phase WFSM model written in phase variables and considering the physical expressions for self and mutual leakage inductances which are provided and experimentally validated in [17].

APPENDIX B

In this Appendix it will be proved that each of the terms which appear in the right-hand side of (4) are determined once $v_{x1a1}(t), v_{p1u1}(t)$ are known.

A. Term $v_{x1c1}(t)$

Based on the first assumption in Section III-A, we can write:

$$v_{x1c1}(t) = v_{x1a1}\left(t + 2\pi/3\omega_m\right). \qquad (B1)$$

B. Terms $v_{\mathrm{ind}}(t)$ and $u_{\mathrm{dcg1}}(t)$

From KVL applied to Fig. 5 we have:

$$v_{\mathrm{ind}}(t) = \tfrac{1}{2}\left\lfloor u_{\mathrm{dcm2}}(t) + u_{\mathrm{dcm1}}(t) - u_{\mathrm{dcg2}}(t) - u_{\mathrm{dcg1}}(t)\right\rfloor \qquad (B2)$$

where u_{dcm1} and u_{dcm2} are the input dc voltages of LCI1 and LCI2, respectively, and u_{dcg1} and u_{dcg2} are the output dc voltages of the two rectifiers.

As regards $u_{\mathrm{dcm2}}(t), u_{\mathrm{dcm1}}(t)$ in (B2), from the second phase shift assumption in Section III-A we have:

$$u_{\mathrm{dcm2}}(t) = u_{\mathrm{dcm1}}\left(t - \pi/6\omega_m\right) \qquad (B3)$$

where

$$\begin{aligned} u_{\mathrm{dcm1}}(t) &= v_{x1a1}(t) - v_{y1a1}(t) \\ &= v_{x1a1}(t) + v_{x1a1}\left(t + \pi/\omega_m\right). \end{aligned} \qquad (B4)$$

In (B4), the equality below has been used:

$$v_{y1a1}(t) = -v_{x1a1}\left(t + \pi/\omega_m\right). \qquad (B5)$$

Equation (B5) can be proved as follows. Let us consider, for example, an instant t_0 in the interval S3$_1$ (see Fig. 7) where T3$_1$ and T2$_1$ are conducting and

$$v_{x1a1}(t_0) = -e_{a1}(t_0) + e_{b1}(t_0). \qquad (B6)$$

180 degrees later, T6$_1$ and T5$_1$ are conducting (interval S6$_1$) and

$$\begin{aligned} v_{y1a1}(t_0 + \pi/\omega_m) &= -e_{a1}(t_0 + \pi/\omega_m) + e_{b1}(t_0 + \pi/\omega_m) \\ &= -[-e_{a1}(t_0) + e_{b1}(t_0)]. \end{aligned} \qquad (B7)$$

So, from (B6) and (B7), we can infer (B5).

The equality (B5) also holds during commutation intervals, i.e.:

$$\Delta v_{y1a1}^{L}(t) = -\Delta v_{x1a1}^{L}\left(t + \pi/\omega_m\right). \qquad (B8)$$

This can be proved by taking commutation intervals C3$_1$ and C6$_1$ as examples (see Fig. 7). During C3$_1$, (15) yields:

$$\begin{aligned} \Delta v_{x1a1}^{L}(t) &= e_{a1}(t) - e_{b1}(t) \\ &\text{with } \omega_m t \in [\theta_0 + 2\pi/3, \theta_0 + 2\pi/3 + \mu]. \end{aligned} \qquad (B9)$$

During C6$_1$ (which is shifted 180 electrical degrees, i.e., π/ω_m seconds, later with respect to C3$_1$) T5$_1$, T6$_1$ and T4$_1$ are conducting simultaneously and $v_{y1a1}(t + \pi/\omega_m)$ is equal to zero because T4$_1$ short-circuits phase terminal $a1$ and point $y1$. If the commutation is not taken into account, during interval S6$_1$ $(\theta_0 + 5\pi/3 < \theta < \theta_0 + 2\pi)$ T6$_1$ is conducting and therefore phase terminal $b1$ is at the same potential as $y1$, hence

$$v_{y1a1}^{0}\left(t + \pi/\omega_m\right) = e_{b1}\left(t + \pi/\omega_m\right) - e_{a1}\left(t + \pi/\omega_m\right). \qquad (B10)$$

Therefore, from (B9) and (B10) we can write:

$$\begin{aligned} \Delta v_{y1a1}^{L}\left(t + \pi/\omega_m\right) &= v_{y1a1}\left(t + \pi/\omega_m\right) - v_{y1a1}^{0}\left(t + \pi/\omega_m\right) \\ &= 0 - [e_{b1}\left(t + \pi/\omega_m\right) \\ &\quad - e_{a1}\left(t + \pi/\omega_m\right)]. \end{aligned} \qquad (B11)$$

Considering the expressions (1) for motor EMF's, it is apparent that

$$\begin{aligned} e_{a1}(t) &- e_{b1}(t) \\ &= -[e_{a1}(t + \pi/\omega_m) - e_{b1}(t + \pi/\omega_m)]. \end{aligned} \qquad (B12)$$

If substituted into (B9) and (B11), this finally proves (B8). With similar reasoning, (B8) can be proved to hold for all the other commutation intervals as well.

As regards $u_{\mathrm{dcg2}}(t), u_{\mathrm{dcg1}}(t)$, with the same reasoning used for $u_{\mathrm{dcm2}}(t), u_{\mathrm{dcm1}}(t)$, we can write (B13) and (B14):

$$u_{\mathrm{dcg2}}(t) = u_{\mathrm{dcg1}}\left(t - \pi/6\omega_g\right) \qquad (B13)$$

$$u_{\mathrm{dcg1}}(t) = v_{p1u1}(t) + v_{p1u1}\left(t + \pi/\omega_g\right). \qquad (B14)$$

C. Term $v_{y2a2}(t)$

Based on the second assumption in Section III-A and based on (B5), we can write:

$$v_{y2a2}(t) = -v_{x1a1}\left(t + \pi/\omega_m - \pi/6\omega_m\right). \qquad (B15)$$

APPENDIX C

In this Appendix the differential equations governing the commutation transient in LCI1 during commutation interval C3$_2$ (see Fig. 7) are investigated. Taking into account both stator and rotor circuits we can write the system of differential equation (C1) at the bottom of the page, where $\Delta v_{a1}^{M}(t), \Delta v_{b1}^{M}(t)$ are the voltage drops across phases $a1$, $b1$ due to the mutual couplings of these phases both with phases $a2$, $b2$ and with rotor circuits. The rotor circuits are the d-axis and q-axis dampers, respectively indicated with subscripts kd and kq and the field circuit, indicated with subscript f. In the calculation of $\Delta v_{a1}^{M}(t), \Delta v_{b1}^{M}(t)$

resistive drops are neglected as usually done [16] and the rotor circuits can be regarded as shorted during the commutation transient [16].

In (C1), L_{kd}^σ, L_{kq}^σ and L_f^σ are the stator-referred leakage inductances of damper and field circuits and $L_{p1,p2}$ is the mutual inductance between phases $p1$ and $p2$ with $p1 \in \{a1,b1,c1\}$ and $p2 \in \{a2,b2,c2\}$. Furthermore, $L_{p,\mathrm{kd}}, L_{p,\mathrm{kq}}, L_{p,f}$ are the mutual inductances between phase $p \in \{a1,b1,c1,a2,b2,c2\}$ and damper and field circuits. In particular, the following equations hold [18]:

$$L_{p1,p2} = L_{p1,p2}^\sigma + (L_{\mathrm{md}} + L_{\mathrm{mq}}) \cos(\theta_{p1} - \theta_{p2})/3$$
$$+ (L_{\mathrm{md}} - L_{\mathrm{mq}}) \cos(2\theta_r - (\theta_{p1} + \theta_{p2}))/3 \quad \text{(C2)}$$

where $L_{p1,p2}^\sigma$ is the leakage inductance between phases $p1, p2$, θ_p is the position of phase p symmetry axis and θ_r is the rotor position. It can be seen from (C2) that $L_{p1,p2}$ depends on the rotor position due to rotor saliency; the expressions of $L_{p,\mathrm{kd}}, L_{p,\mathrm{kq}}, L_{p,f}$ are also dependent on θ_r according to the equations below [18]:

$$L_{p,\mathrm{kd}} = L_{p,f} = L_{\mathrm{md}} \cos(\theta_p - \theta_r)$$
$$L_{p,\mathrm{kq}} = L_{\mathrm{mq}} \sin(\theta_p - \theta_r). \quad \text{(C3)}$$

From (29) we have:

$$di_{a2}/dt = -di_{b2}/dt = -di_2/dt. \quad \text{(C4)}$$

By substituting (C2), (C3) and (C4) into (C1) and after some algebraic manipulations, the effect of the commutation during $C3_2$ on the voltage drops $\Delta v_{a1}^M(t)$, $\Delta v_{b1}^M(t)$ is found to be expressed by the following equation:

$$\Delta v_{a1}^M(t) = M_{\mathrm{eq},a1} di_2/dt, \quad \Delta v_{b1}^M(t) = M_{\mathrm{eq},b1} di_2/dt \quad \text{(C5)}$$

where

$$M_{\mathrm{eq},a1} = \left(-L_{a1,a2}^\sigma + L_{a1,b2}^\sigma\right) - \sqrt{3}\left(L_d''' + L_q'''\right)/3$$
$$-\sqrt{3}\left(L_d''' - L_q'''\right)\cos(2\theta_r)/3$$
$$M_{\mathrm{eq},b1} = \left(-L_{b1,a2}^\sigma + L_{b1,b2}^\sigma\right) + \sqrt{3}\left(L_d''' + L_q'''\right)/6$$
$$-\sqrt{3}\left(L_d''' - L_q'''\right)\sin(2\theta_r - \pi/6)/3 \quad \text{(C6)}$$

being L_d''', L_q''' given by (33). From the physical point of view, the mutual inductances (C6) account for the magnetic coupling between the closed loop where the commutation current i_2 flows and the phases $a1$, $b1$ respectively.

Observing that during $C3_2$ (see Fig. 10) we have $\Delta v_{x1a1}^M(t) = \Delta v_{b1}^M(t) - \Delta v_{a1}^M(t)$ since $T3_1$ is conducting, according to (C5)

one can write

$$\Delta v_{x1a1}^M(t) = M_{\mathrm{eq},b1} di_2/dt - M_{\mathrm{eq},a1} di_2/dt = M_{\mathrm{eq}} di_2/dt,$$
$$\text{(C7)}$$

having defined M_{eq} as:

$$M_{\mathrm{eq}} = M_{\mathrm{eq},b1} - M_{\mathrm{eq},a1} = \left[L_{a1,a2}^\sigma - L_{a1,b2}^\sigma - L_{b1,a2}^\sigma\right.$$
$$\left. + L_{b1,b2}^\sigma + \sqrt{3}\left(L_d''' + L_q'''\right)/2\right.$$
$$\left. + \left(L_d''' - L_q'''\right)\cos(2\theta_r + \pi/6)\right]. \quad \text{(C8)}$$

As regards the leakage inductances in (C8), we have that the phase shift between phases $a1$, $a2$ is the same (30 electrical degrees) as between phases $b1$, $b2$; furthermore, the phase shift between $a1$ and $b2$ is $180-30 = 150$ electrical degrees while phases $b1$ and $a2$ are orthogonal, hence [17]:

$$L_{a1,a2}^\sigma = L_{b1,b2}^\sigma = -L_{a1,b2}^\sigma, \quad L_{b1,a2}^\sigma = 0. \quad \text{(C9)}$$

By taking (C9) into account, we can derive the expression for M_{eq} as

$$M_{\mathrm{eq}} = 3L_{a1,a2}^\sigma + \frac{\sqrt{3}}{2}\left(L_d''' - L_q'''\right)$$
$$+ \left(L_d''' - L_q'''\right)\cos(2\theta_r + \tfrac{\pi}{6}). \quad \text{(C10)}$$

Although the exact expression of M_{eq} depends on the rotor position, the term $L_d''' - L_q'''$ is typically much smaller than the term $3L_{a1,a2}^\sigma + \frac{\sqrt{3}}{2}\left(L_d''' + L_q'''\right)$. For instance, in case of the example machine whose parameters are given in Appendix A, the latter term is nearly 14 times greater than the former. Hence, we can treat M_{eq} as a constant and approximate it as per (32).

REFERENCES

[1] R. Bhatia, H. Krattiger, A. Bonanini, D. Schafer, J. T. Inge, and G. H. Sydnor, "Adjustable speed drive using a single 135 000 HP synchronous motor," *IEEE Trans. Energy Convers.*, vol. 14, no. 3, pp. 571–576, Sep. 1999.

[2] A. N. Alcaso and A. J. M. Cardoso, "Remedial operating strategies for a 12-pulse LCI drive system," *IEEE Trans. Ind. Electron.*, vol. 55, no. 5, pp. 2133–2139, May 2008.

[3] B. Wu, J. Pontt, J. Rodríguez, S. Bernet, and S. Kouro, "Current-source converter and cycloconverter topologies for industrial medium-voltage drives," *IEEE Trans. Ind. Electron.*, vol. 55, no. 7, pp. 2786–2797, Jul. 2008.

$$\begin{cases} \Delta v_{a1}^M(t) = L_{a1,a2} di_{a2}/dt + L_{a1,b2} di_{b2}/dt + L_{a1,\mathrm{kd}} di_{\mathrm{kd}}/dt + L_{a1,\mathrm{kq}} di_{\mathrm{kq}}/dt + L_{a1,f} di_f/dt \\ \Delta v_{b1}^M(t) = L_{b1,a2} di_{a2}/dt + L_{b1,b2} di_{b2}/dt + L_{b1,\mathrm{kd}} di_{\mathrm{kd}}/dt + L_{b1,\mathrm{kq}} di_{\mathrm{kq}}/dt + L_{b1,f} di_f/dt \\ 0 = L_{kd,a2} di_{a2}/dt + L_{kd,b2} di_{b2}/dt + \left(L_{\mathrm{kd}}^\sigma + L_{\mathrm{md}}\right) di_{\mathrm{kd}}/dt + L_{\mathrm{md}} di_f/dt \\ 0 = L_{kq,a2} di_{a2}/dt + L_{kq,b2} di_{b2}/dt + \left(L_{\mathrm{kq}}^\sigma + L_{\mathrm{mq}}\right) di_{\mathrm{kq}}/dt \\ 0 = L_{f,a2} di_{a2}/dt + L_{f,b2} di_{b2}/dt + L_{\mathrm{md}} di_{\mathrm{kd}}/dt + \left(L_f^\sigma + L_{\mathrm{md}}\right) di_f/dt \end{cases} \quad \text{(C1)}$$

[4] C. A. Wade and D. R. Crane, "Reliability features of large load commutated inverter drives and some cautions in their application," *IEEE Trans. Ind. Appl.*, vol. IA-19, no. 4, pp. 534–540, Jul./Aug. 1983.

[5] J. Song-Manguelle, C. Sihler, and S. Schramm, "A general approach of damping torsional resonance modes in multi-megawatt applications," *IEEE Trans. Ind. Appl.*, vol. 47, no. 3, pp. 1390–1399, May/Jun. 2011.

[6] A. Tessarolo, S. Castellan, R. Menis, and G. Ferrari, "On the modeling of commutation transients is split-phase synchronous motors supplied by multiple load-commutated inverters," *IEEE Trans. Ind. Electron.*, vol. 57, no. 1, pp. 35–43, Jan. 2010.

[7] B. Singh, S. Singh, and S. P. H. Chender, "Harmonic mitigation in LCI-fed synchronous motor drives," *IEEE Trans. Energy Convers.*, vol. 25, no. 2, pp. 369–380, Jun. 2010.

[8] E. Levi, R. Bojoi, F. Profumo, H. A. Toliyat, and S. Williamson, "Multiphase induction motor drives—A technology status review," *IET Elect. Power Appl.*, vol. 1, no. 4, pp. 489–516, Jul. 2007.

[9] D. A. Paice, *Power Electronic Converter Harmonics: Multipulse Methods for Clean Power*. Piscataway, NJ, USA: IEEE Press, 1996.

[10] K. S. Smith and L. Ran, "Torsional resonance risk management in islanded industrial power systems supplying large VFDs," *IEEE Trans. Ind. Appl.*, vol. 44, no. 6, pp. 1841–1850, Nov./Dec. 2008.

[11] S. Schramm, C. Sihler, J. Song-Manguelle, and P. Rotondo, "Damping torsional interharmonic effects of large drives," *IEEE Trans. Power Electron.*, vol. 25, no. 4, pp. 1090–1098, Apr. 2010.

[12] A. Tessarolo, C. Bassi, G. Ferrari, D. Giulivo, R. Macuglia, and R. Menis, "Investigation into the high-frequency limits and performance of load commutated inverters for high-speed synchronous motor drives," *IEEE Trans. Ind. Electron.*, vol. 60, no. 6, pp. 2147–2157, Jun. 2013.

[13] H. Atighechi, S. Chiniforoosh, K. Tabarraee, and J. Jatskevich, "Average-value modeling of synchronous-machine-fed thyristor-controlled-rectifier systems," *IEEE Trans. Energy Convers.*, vol. 30, no. 2, pp. 487–497, Jun. 2015.

[14] L. Hu and R. Yacamini, "Harmonic transfer through converters and HVDC links," *IEEE Trans. Power Electron.*, vol. 7, no. 3, pp. 514–524, Jul. 1992.

[15] S. Mohamadian, A. Tessarolo, and A. Shoulaie, "Design of an efficient starting circuit for LCI-fed synchronous motor drives," in *Proc. 5th Power Electron. Drive Syst. Technol. Conf.*, 5–6 Feb., 2014, pp. 31–36.

[16] B. K. Bose, *Power Electronics and AC Drives*. Englewood Cliffs, NJ, USA: Prentice-Hall, 1986.

[17] A. Tessarolo and D. Giulivo, "Analytical methods for the accurate computation of stator leakage inductances in multiphase synchronous machines," in *Proc. Int. Symp. Power Electron., Elect. Drives, Autom. Motion*, Pisa, Italy, Jun. 14–16, 2010, pp. 845–852.

[18] A. Tessarolo and S. Castellan, "Analytical and circuital modelling of commutation transients in phase-split synchronous motors supplied by multiple load commutated inverters," in *Proc. 18th Int. Conf. Elect. Mach.*, Vilamoura, Portugal, Sep. 6–9, 2008, pp. 1–8.

Simone Castellan received the Laurea and Ph.D. degrees in electrical engineering from the University of Padova, Padova, Italy. In 2000, he joined the University of Trieste, Trieste, Italy, as a Researcher dealing with electric power converters, machines, and drives. He is currently an Assistant Professor of Power Electronics with the University of Trieste. His main research interests include the field of power converters for harmonic and flicker compensation, medium-voltage drives, fault tolerant drives, renewable energy sources, and all-electric ships.

Alberto Tessarolo (M'06–SM'15) received the Laurea and Ph.D. degrees in electrical engineering from the University of Trieste, Trieste, Italy, in 2000, and from the University of Padova, Padova, Italy, in 2011, respectively. Until 2006, he worked in the design and development of innovative motors and generators for high power applications with NIDEC-ASI (formerly Ansaldo Sistemi Industriali). He is currently with the Engineering and Architecture Department, University of Trieste, Italy, where he teaches the electric machine design course. His main research interests include the area of electric machine and drive modeling, design and analysis, a field in which he has authored more than 100 scientific papers. He acts as the Principal Investigator for various research projects in cooperation with leading electric machine manufacturers and final users, including the Italian Navy. He serves as an Editor for the IEEE TRANSACTIONS ON ENERGY CONVERSION and as an Associate Editor for the IEEE TRANSACTIONS ON INDUSTRY APPLICATIONS. He is a Registered Professional Engineer in Italy.

Giancarlo Ferrari was born in Bergamo, Italy, in 1982. He received the Laurea (Hons.) degree in electrical engineering from the Polytechnic University of Milan, Milan, Italy, in 2007. He is currently working with NIDEC-ASI, Milan, as a Research and Development Engineer. His main research interests include medium-voltage load commutated inverters for high-power synchronous machine variable-frequency drives.

Sobhan Mohamadian received the B.Sc. and M.Sc. degrees from the Iran University of Science and Technology, Tehran, Iran, in 2007 and 2010, respectively, where he is currently working toward the Ph.D. degree in electrical engineering. His research interests include power quality, power electronics, and electrical machines. Between February 2014 and March 2015, he spent a period as a Visiting Scholar at the University of Trieste, Trieste, Italy, where he worked on research projects regarding high-power multiphase motor drives, and multiphase machine modeling and analysis. Mr. Mohamadian is a Member of Iran's National Elite Foundation.

Abbas Shoulaie was born in Isfahan, Iran, in 1949. He received the B.Sc. degree from the Iran University of Science and Technology (I.U.S.T.), Tehran, Iran, in 1973, and the M.Sc. and Ph.D. degrees in electrical engineering from Université des Sciences et Techniques du Languedoc, Montpellier, France, in 1981 and 1984, respectively. He is currently a Professor of Electrical Engineering with I.U.S.T. His research interests include power electronics, magnetic systems and linear motors, flexible ac current transmission systems, and high voltage dc.